Original article

Mechanical properties of nodular natural gas hydrate-bearing sediment

Yujing Jiang[1,2], Ruiqi Zhang[1], Ruijie Ye[1], Kang Zhou[1], Bin Gong[1]*, Naser Golsanami[1]*

[1]*State Key Laboratory of Mining Disaster Prevention and Control Co-founded by Shandong Province and the Ministry of Science and Technology, Shandong University of Science and Technology, Qingdao 266590, P. R. China*
[2]*Graduate School of Engineering, Nagasaki University, Nagasaki 8528521, Japan*

Abstract:
Natural gas hydrate is a relatively realistic alternative energy source to conventional fossil fuels with considerable reserves. Natural gas hydrate sediments are widely distributed in marine sediment on continental margins. In this study, a numerical modeling method for sediment containing nodular gas hydrates is developed using the two-dimensional discrete element simulation software. The effects of saturation, confining pressure, and nodule radius on the mechanical properties of heterogeneous nodular gas-hydrate-bearing sediment were analyzed using the stress-strain, fracture development, and partial body strain curves, as well as force chain distribution. The results indicated that the mechanical strength of sediment containing round nodular gas hydrates was proportional to the gas hydrate saturation and simulated confining pressure. When hydrate saturation was low, the failure strength of the gas-hydrate-bearing sediment diminished as the nodule radius increased. The simulations showed that variations in sediment porosity influenced the development and evolution of the shear band, resulting in higher porosity around the shear band. These results were analyzed from the perspectives of saturation and confining pressure to determine the failure and deformation law of simple nodular gas hydrate-bearing sediment and provide theoretical support for the subsequent study of the exploitation method of shallow buried deep gas hydrates.

1. Introduction

Natural gas hydrate (NGH) is a type of cage crystalline compound that forms from natural gas and water under low temperature and high pressure conditions in the marine environment (Sloan, 2003; Hyodo et al., 2013; Aregbe, 2017). Since the discovery of NGH in 1810 (Makogon et al., 2007), its mechanical properties have been studied thoroughly. Previous studies have reported that the carbon content of NGH is twice that of conventional fossil fuels (Demirbas, 2010; Seol and Lee, 2013). In addition, NGH releases large amounts of heat after combustion, indicating its importance role as a potential energy source (Collett and Kuuskraa, 1998; Wang et al., 2021b). NGH-bearing sediments are considered a viable alternative energy source, alongside shale gas, coalbed methane, and other unconventional oil and gas reservoirs, owing to their

environmentally benign nature post-combustion (Whiticar et al., 1986; Kumar and Sonawane, 2004; Moridis et al., 2011). Fig. 1 show the global distribution and resource reserves of gas hydrate resources explored thus far.

Previous studies (Li et al., 2021b) have determined that NGHs occur in various states within reservoirs owing to their complex formation environment. Based on the contact between the hydrate and sediment, some researchers have divided hydrates into pore infiltration and particle displacement types (Ning et al., 2020), the distributions of which are shown in Fig. 2. For instance, a significant portion of the hydrate resources found in the Dongsha and Qiongdongnan sea areas occur as nodules, veins, and layers within the sediment (Dong et al., 2023; Wang et al., 2023), all of which are particle-displaced NGHs. Most extruded gas hydrates are nodular gas hydrates. Compared with pore infiltration-type gas hydrates,
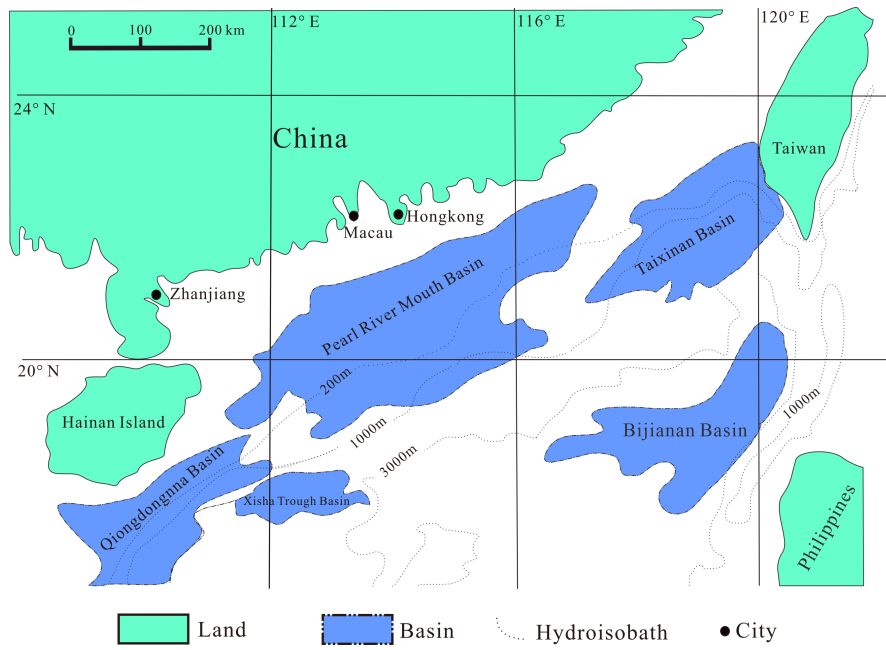
Fig. 1. Distribution of NGH resources in the Shenhu area of the South China Sea (Collett, 2002; Wang et al., 2021a).
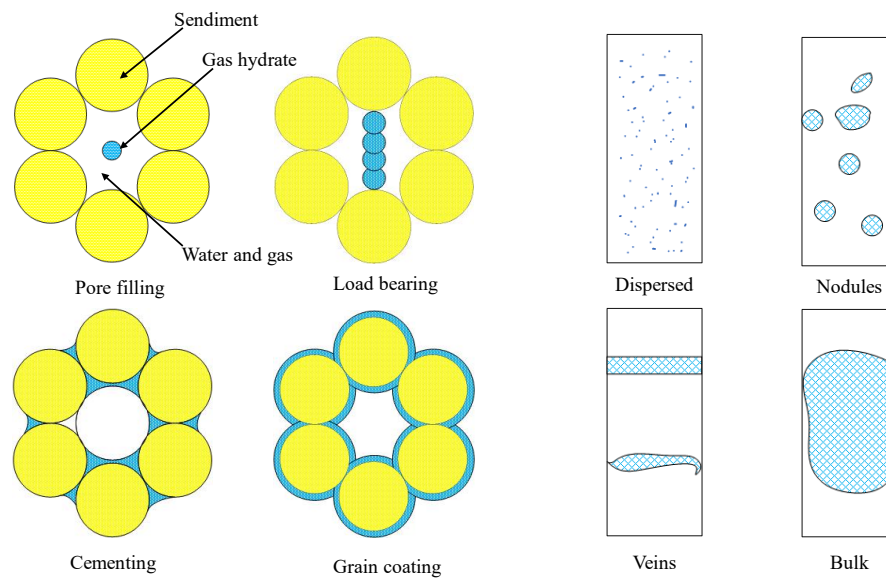
Fig. 2. Occurrence state of the proved hydrate resources at present (Wang et al., 2021a).

nodular gas hydrates are visible to the naked eye in the sediment, and the contact between hydrate and sediment is a clear dividing line. The distribution of nodular NGHs is relatively dense and the cavities that form after the decomposition of nodular NGHs are large, resulting in geological problems caused by reservoir instability. In addition, mining difficulties are relatively high, and the mechanical properties of nodular NGH-bearing sediment also differ from those of pore-infiltrated NGHs. However, previous studies have mostly addressed the mechanical properties of pore-infiltrated NGH-bearing sediment and have not focused on nodular NGH-bearing sediment (Yoneda et al., 2019). Thus, the physical and mechanical properties of such deposits have not been studied sufficiently.

Since NGHs form under various environmental conditions as different types with differing mechanical properties, studying the mechanical properties of NGH-bearing sediment under different conditions is crucial for their future safe and efficient exploitation and development (Brugada et al., 2010; Linga and Clarke, 2016). NGHs can be divided into pore-filling, cementing, supporting, and mixed types (Zhang et al., 2015; Li et al., 2021a; You et al., 2022; Bai et al., 2023). Some researchers have divided NGHs into pore permeability and particle exclusion types based on the effective particle stress and capillary pressure difference in the pores (Dai and Seol, 2014; Wang et al., 2021a).

Previous studies have extensively investigated the mechanical properties of the various NGH types (Zeng et al., 2021;

You et al., 2022; Zhang et al., 2022; Zhao et al., 2022; Wu et al., 2023). Laboratory tests and numerical simulations have supplemented and improved the failure and deformation law of NGH-bearing sediment from microscopic to mesoscopic to macroscopic scales. Masui et al. (2008) compared laboratory-synthesized gas hydrate and NGH-bearing sediment and found that they exhibited extremely similar mechanical properties. Hyodo et al. (2009) investigated the failure and deformation law of NGH-bearing sediment by performing tri-axial tests under different conditions and found that the NGH strength was related to saturation, temperature, and confining pressure but was not related to the effective stress. Winters et al. (2007) also conducted laboratory tri-axial and acoustic emission tests to study the effects of porosity on sound velocity and shear strength in NGH-bearing sediment by preparing hydrate-bearing sediment samples with different porosities. Madhusudhan et al. (2019) studied the effects of hydrate cementation on granular materials with different specific surface areas and particle shapes. Their results indicate that particle size, surface area, and shape are the main factors that affect the failure strength of NGH-bearing sediment, among which particle size considerably affects the sediment strength. Priest et al. (2019) conducted tri-axial tests on the geomechanical properties of NGH-bearing sediment recovered from the Bay of Bengal. Miyazaki et al. (2010) performed tri-axial tests on CO_2 hydrate-bearing sediment to determine the differences in mechanical properties between CO_2 hydrate- and CH_4 hydrate-bearing sediment, which provided a reference for laboratory synthesis of simple CO_2 hydrate-bearing sediment. Rutqvist et al. (2009) examined the mechanical properties of an NGH layer during step-down exploitation and concluded that the likelihood of shear failure was dependent on the initial stress state and geomechanical characteristics of the reservoir. The Poisson's ratio of the gas hydrate layer was crucial in determining whether the changes in reservoir stress would increase or decrease the likelihood of shear failure. Zhang et al. (2010) proposed using tetrahydrofuran hydrate, which has a more stable occurrence and simplified synthesis method, to replace NGHs in laboratory tests. During analysis, they concluded that the sediment strength decreased considerably as the hydrate decomposed. Li et al. (2011b) studied the effect of confining pressure on the mechanical properties of hydrate-bearing sediment and concluded that, at low confining pressures, the failure strength of hydrate-bearing sediment increased proportionally with increasing confining pressure. Li et al. (2021a) conducted tri-axial tests on sediment samples from the South China Sea with varying hydrate saturation levels and found that the sediment stress-strain curves exhibited strain-softening phenomena after testing. In addition, the partial stress of the hydrate-bearing sediment increased with increasing hydrate saturation and effective confining pressure. Methods for studying the mechanical properties of NGH-bearing sediment are continuously evolving. In this study, we used a numerical simulation method based on the widely used PFC2D discrete element simulation software. Previously, Vinod et al. (2014) proposed a two-dimensional discrete element modeling method for NGH-bearing sediment. In addition, Jiang et al. (2017) constructed a model

of NGH-bearing sediment using a discrete element numerical simulation and tri-axial simulation tests by determining the relationship between the macro- and micro-parameters. This method allowed them to simulate the hydrate loading mode under varying temperatures and reverse pressures. Gong et al. (2022) studied the energy changes during gas hydrate decomposition using discrete element numerical simulations and performed corresponding two-dimensional discrete element modeling of dispersed gas hydrate-bearing sediment. Jiang and Gong (2020) investigated the effects of saturation, friction angle, and confining pressure on the mechanical properties of gas hydrate-bearing sediment. Gong et al. (2020) studied the effects of a flexible boundary on the mechanical properties of NGH-bearing sediment using the PFC2D software and found that discrete element simulations can accurately represent the macroscopic mechanical properties of hydrate-bearing sediment and sand samples under undrained conditions. Yang and Zhao (2014) constructed a three-dimensional model of gas hydrate-bearing sediment using the PFC3D software and performed corresponding tri-axial simulations. Their results indicate that discrete element simulation can accurately represent the principal mechanical properties of gas hydrate-bearing sediment and that changes in the cementation properties between NGH and sand particles will impact the mechanical properties of gas hydrate-bearing sediment. Most of these studies focused on the type of particle exclusion and pore wettability, which are mechanical properties of dispersed gas hydrate-bearing sediment.

Few studies have investigated the mechanical properties of nodular gas hydrates in the southeastern South China Sea, particularly those of nodular and massive gas hydrate-bearing sediment in the Shenhu and Qiong regions which are extremely rich in reserves and have high research value (Wang et al., 2021a; Wan et al., 2023). Therefore, we developed a discrete element model for sediment containing nodular gas hydrates and performed corresponding numerical simulations.

The results were analyzed from the perspectives of saturation and confining pressure to determine the failure and deformation law of simple nodular gas hydrate-bearing sediment and provide theoretical support for the subsequent study of the exploitation method of shallowly buried deep gas hydrates.

2. Numerical modeling methods

In this study, the PFC2D discrete element simulation software package (Itasca Company) was used to perform biaxial simulations of sediment containing nodular gas hydrates and analyze the simulation results.

2.1 Model construction

The skeleton composition and hydrate particles in the nodular gas hydrate-bearing sediment in the simulations were replaced with small spherical particles, and the hydrate nodules had simple geometric shapes. The model boundary was specified as a rectangle with dimensions of 0.8 mm × 1.6 mm. Based on the results of Jensen et al. (1999), the size effect can be overlooked when the average particle size of the simulated sample is 30 and the total number of particles in the sample

$S_h = 0\%$　　　　$S_h = 10\%$　　　　$S_h = 20\%$　　　　$S_h = 30\%$　　　　$S_h = 40\%$　　　　$S_h = 100\%$
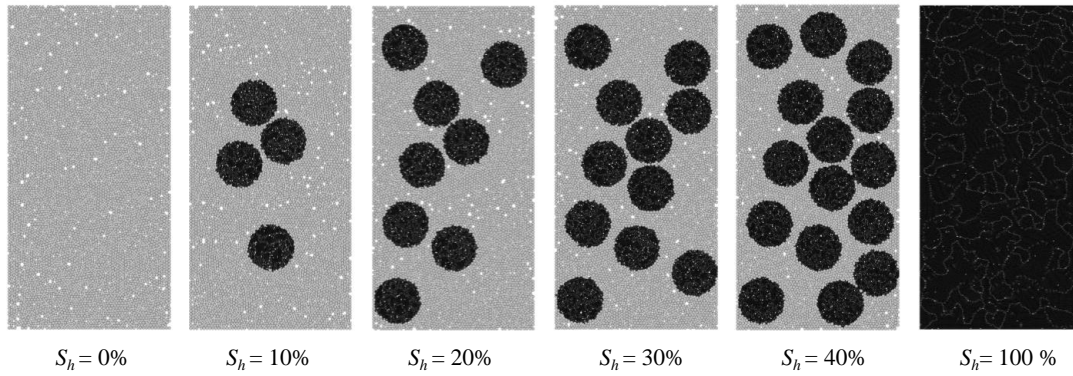
Fig. 3. Numerical model of nodular gas hydrate-bearing sediments under different hydrate saturation conditions.

(a)　　　　　　　　　　　　(b)
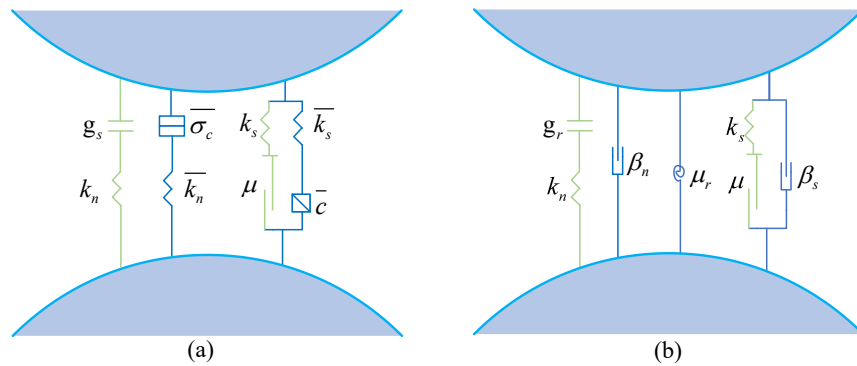
Fig. 4. Contact type: (a) linear parallel bond model logic diagram and (b) rolling resistance linear model logic diagram (Itasca, 2018).

exceeds 2,000.

As hydrates form in the sediment skeletal pores, the hydrate particles are typically much smaller than sand particles. According to the ratio of sand to hydrate particles determined by Gong et al. (2020), the sand particle size in this study was set to 0.006-0.008 mm, with a density of 2,650 kg/m^2, and the hydrate particle size was set to 0.002 mm, with a density of 900 kg/m^2. First, a rigid block was randomly generated within the model range, from which a numerical model consisting only of sand particles and rigid blocks was generated. The rigid block was transformed into a fillable region, which was filled with small spheres (representing hydrate particles) to obtain a numerical model of a gas hydrate-bearing sediment containing nucleation. Hydrate saturation was determined by the number of particulates produced. The model's outer boundary was then served to ensure the equilibrium of the interior. Fig. 3 shows a portion of the numerical model output.

2.2 Contact model parameters

Since cementation between hydrate particles must be taken into account, a linear parallel bond model was used for cementation between hydrate particles and between hydrate and sand particles. Since a cementing force was present between the particles, the cementation between the particles disappeared and cracks formed when the stress exceeded the cementing force. The structure of the model is shown in Fig. 4(a). A linear rolling resistance model was used between the sand grains (Fig. 4(b)). The shape effect of the sand particles in the sample and the rolling resistance between the particles were considered in the construction of the model. Different contact modes were used to simulate the contact between the hydrate and sand particles. The specific contact model parameters are listed in Table 1.

2.3 Feasibility analysis

The parameters should be calibrated before running the numerical simulation, as the corresponding results for pure NGH-bearing sediment at 100% saturation have not yet been determined. As tetrahydrofuran hydrate and NGH have similar physical properties, many researchers believe that tetrahydrofuran hydrate can theoretically replace NGH in laboratory studies (Zhang et al., 2010; Li et al., 2011a; Liu et al., 2018). Therefore, parameter calibration was based on the results of laboratory analyses of the mechanical properties of hydrate-bearing sediment (Yun et al., 2007; Yoneda et al., 2019), as well as numerical simulations (Yang and Zhao, 2014; Jiang et al., 2019; Jiang and Gong, 2020). Fig. 5 shows the stress-strain curves of the laboratory and simulated results under identical saturation and confining pressure conditions. The simulated results were comparable to those of the laboratory analyses and can therefore be used for data analysis instead of the laboratory results.

Table 1. Contact parameters.

Contact group	Contact type	Contact parameter	
Hydrate-Hydrate	Linearbond	Emod (Pa): 2×10^8	Pb_coh (Pa): 3×10^6
		Kratio: 1.42	Pb_fa (°): 10
		Pb_ten (Pa): 2×10^6	Fric: 0.15
Hydrate-Soil	Linearbond	Emod (Pa): 2×10^8	Pb_coh (Pa): 3×10^6
		Kratio: 1.42	Pb_fa (°): 10
		Pb_ten (Pa): 2×10^6	Fric: 0.15
Soil-Soil	Rrlinear	Emod (Pa): 1×10^8	Fric: 0.5
		Kratio: 1.0	Rr_fric: 0.6
Ball-Face	Linear	Emod (Pa): 1×10^8	Kratio: 1.0
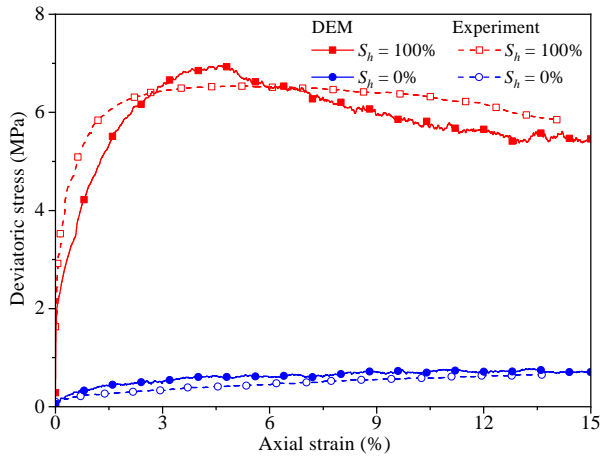
Fig. 5. Comparison of numerical simulation and experiment results.

2.4 Simulation schemes

In this simulation, the mechanical properties and failure deformation laws of nodule-bearing gas hydrate sediments were studied from four parts: hydrate saturation, effective confining pressure, nodule size, and evolution mechanism of the shear zone.

Hydrate saturation (S_h) is defined as the proportion of hydrate in sediment pores. However, for nodular gas hydrate sediments, this study redefines saturation as the ratio of the total hydrate area to the total area of the two-dimensional model. The specific research methods were as follows: by changing the number of nodules in the model to simulate different saturation conditions, and attempting to ensure that the distribution and morphology of nodules had small differences, the mechanical properties of the nodular gas hydrate-bearing sediment were simulated at a constant confining pressure (1 MPa) and different hydrate saturations, the simulation results were drawn and analyzed.

According to the model conditions and the laboratory tests performed by Li et al. (2011b), confining pressures (σ_c') of 1-3 MPa, and 5 MPa were used for the simulation. The stress-strain curves and fracture development curves under different confining pressure conditions were plotted from the simulation results, the stress-strain relationship of the model under different confining pressure conditions was analyzed, and the influence of confining pressure on the fracture development inside the model was analyzed. The influence of confining pressure on the mechanical strength of the model is revealed.

Different saturation and confining pressure conditions are suitable for investigating the failure and deformation laws of gas hydrate-bearing sediment at almost all conditions. However, the effects of nodule shape, size, and distribution on the failure and deformation laws of nodular gas hydrate-bearing sediment should be considered because only round nodules were considered in this study. Therefore, we investigated the effect of nodule size (*d*) on the mechanical properties of NGH-bearing sediment. In this simulation, three models with different nodular particle sizes, 0.22, 0.16, and 0.10 mm, were selected for simulation experiments, and the hydrate saturation remained unchanged by changing the number of nodules in the model, and simultaneously, the distribution morphology of hydrate between the three models was not considerably different.

Through the above simulation methods, the simulation result curves were drawn, including stress-strain curves, fracture development curves, and volumetric strain curves, analyzed the trend of the curves and obtained the influence of different influencing factors on the mechanical properties and failure deformation law of nodule-containing gas hydrate sediments.

3. Results and discussion

3.1 Saturation effect

The stress-strain curves, shown in Fig. 6, indicate that with the increase of saturation, the peak deviation stress of the stress-strain curve increased, and the maximum stress required for model failure also increased. The higher the saturation, the more apparent would be the softening phenomenon of the curve; this also indicates that the higher the saturation, higher would be the mechanical strength of the heterogeneous
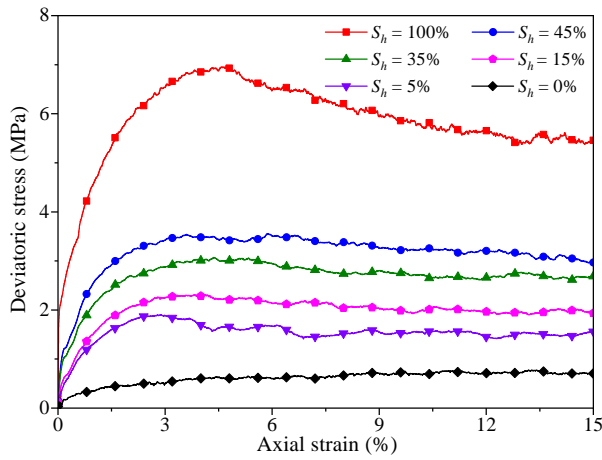
Fig. 6. Stress-strain curves with different hydrate saturation conditions under 1 MPa confining pressure.
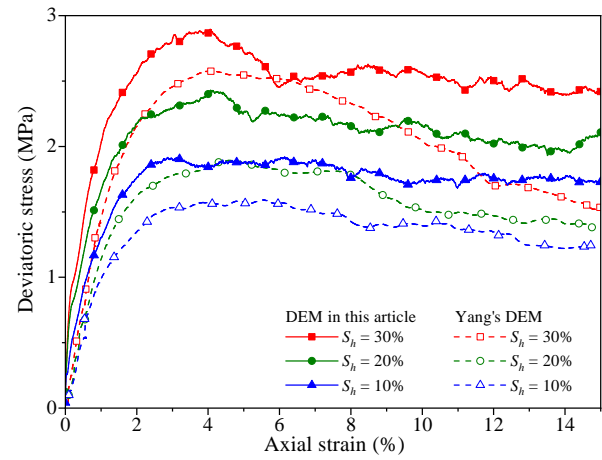
Fig. 7. Comparison between numerical simulation results in this article and Yang's.

nodular NGH-bearing sediment.

To verify the differences between the failure and deformation laws of nodular and pore gas hydrate-bearing sediment, some of the simulation results obtained in this study were compared with those of Yang and Zhao (2014), who investigated the failure and deformation laws of dispersed gas hydrate-bearing sediment (Fig. 7). At a confining pressure of 1 MPa, the stress required to reach failure of the hydrate-bearing sediment model increased with increasing saturation. The maximum stress also increased, as did the axial strain required to reach the maximum stress. The strain-softening phenomenon also became more apparent as the saturation increased. These results are comparable to those of a three-dimensional discrete element model of dispersed gas hydrate-bearing sediment (Yang and Zhao, 2014).

According to the force chain diagram model shown in Fig. 8, the distribution of nodular gas hydrate deposits was more concentrated and the contacts between particles were closer than those in dispersed gas hydrate deposits. Under the same confining pressure, the stress required to induce failure at the same saturation was higher in a nodular deposit; however, the overall trend was the same. The saturation of the hydrate-bearing sediment determines the hydrate's resistance to destruction to a certain extent, and these two parameters were directly proportional.

According to the volume strain curve for nodular gas hydrate-bearing sediment at different saturations (Fig. 9), the volume variation law was generally consistent, in which the gas hydrate-bearing sediment first shrank, and then expanded, and higher hydrate saturation yielded more pronounced shear expansion. The shear expansion effect of the hydrate saturation was not evident at 0-5% but became more apparent as the saturation increased.

Simulations revealed that as the axial strain increased, shear and tensile cracks progressively emerged within the model. Notably, the pattern of cracks differed significantly in models with varying hydrate saturations, even when subjected to identical simulation conditions. Therefore, to explore the relationship between saturation and crack development in the model, it obtained the stress-strain curve and the fracture de-

velopment curve at S_h = 35% (Fig. 10). Fig. 10 shows that the hydrate-bearing sediment did not initially produce cracks; however, cracks were produced slowly as the simulation progressed. This curve corresponds to the compaction stage in the stress-strain curve; owing to the limited computing power of the software, the compaction stage in the simulation cannot be represented on the curve. Consequently, the compaction stage was not visible in Fig. 10, and the contacts between the hydrate particles were closer during this stage. By increasing the axial strain, crack development in the hydrate specimens increased continuously toward a fixed value, corresponding to the elastic stage on the stress-strain curve, and the number of cracks increased continuously. The velocity of the crack occurrence tended to be stable, corresponding to the yield stage on the stress-strain curve. When the axial strain increased, the speed of crack production decreased, and the total number of cracks continued to increase. This corresponded to the softening stage on the stress-strain curve.

According to the types and the number of cracks in the model with different saturation degrees (Table 2), higher hydrate saturation produced more fractures and higher hydrate-bearing sediment strength, which is comparable to the results of another study (Gong et al., 2020) on dispersed gas hydrate-bearing sediments. Thus, the mechanical properties of dispersed and nodular gas hydrate-bearing sediments were similar, that is, at the same confining pressure, the failure strengths of both types increased as the saturation increased.

However, in contrast to fracture development in nodular gas-hydrate-bearing sediment, the fracture development curve of the dispersed gas-hydrate-bearing sediment indicates that the fractures formed were mainly shear cracks. Shear cracks were substantially more prevalent than tensile cracks, potentially because the hydrate particles in the dispersed gas hydrate-bearing sediment were in direct contact with sand particles.

Previous experiments have shown that shear cracks often occur when hydrate particles are in contact with sand particles, whereas tensile cracks primarily form between adjacent hydrate particles. However, because the nodules were composed entirely of hydrate particles, which were close together, most
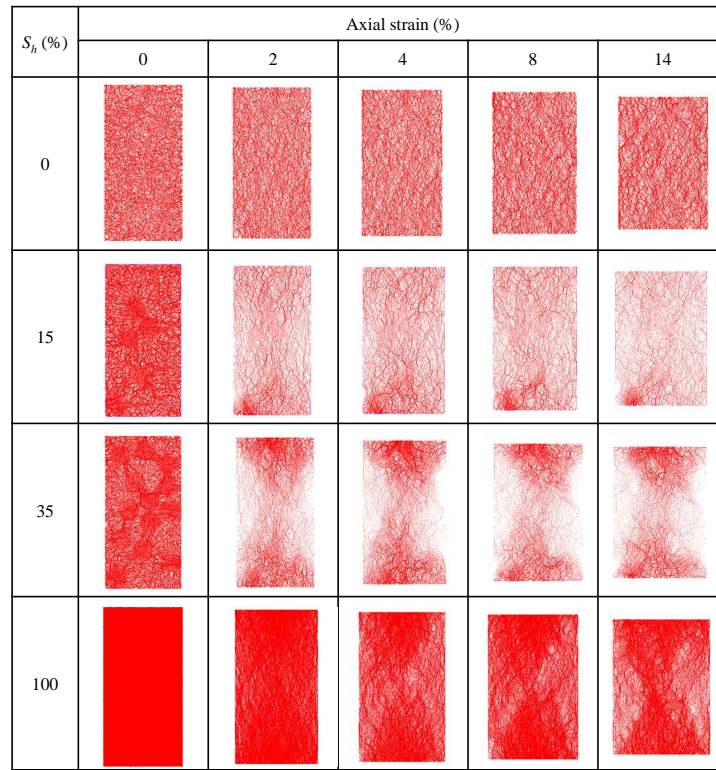
Fig. 8. Change of contact force chain during simulation of samples under different hydrate saturation conditions.
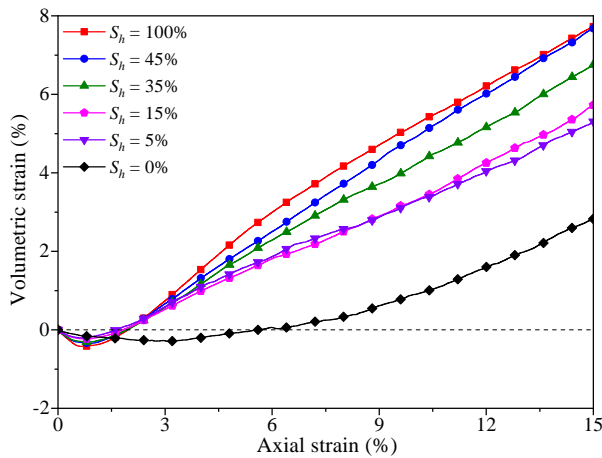
Fig. 9. Volume strain curves for numerical simulation of models under different hydrate saturation conditions.
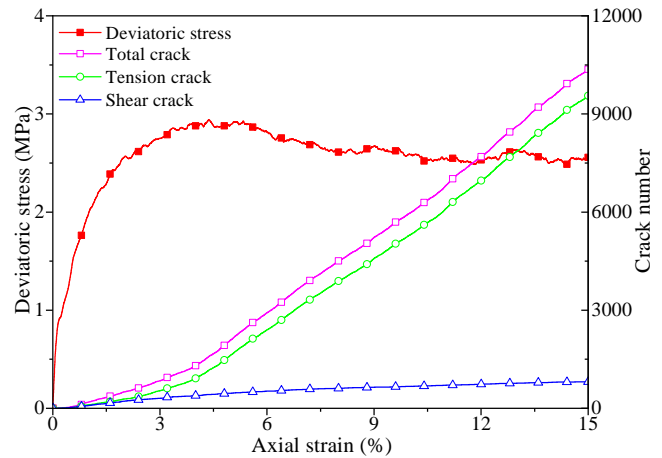
Fig. 10. Stress-strain curve and the development of cracks within the model at $S_h = 35\%$.

cracks generated in the nodular hydrate-bearing sediment were tensile cracks. Fracture distribution maps of the simulated samples with different saturations are shown in Fig. 11. Shear cracks were only observed at the boundary where hydrate nodules were in contact with sand particles, and more shear cracks than tensile cracks developed. This disparity became more pronounced as the saturation increased. When $S_h < 15\%$, as evident from the figure, the cracks were mainly generated around the nodules, and when $S_h \geq 15\%$, cracks appeared inside the nodules. With further increase of saturation, cracks were increasingly generated inside the nodules, and an apparent shear zone was formed. It found that at the end of the

simulation, models with different saturation degrees exhibited a common cracking pattern. Most cracks originated in the nodules at the model's center. Nodules farther from the center produced fewer cracks. However, the nodules near the model's corners showed a higher number of cracks compared to those neither at the center nor corners. This pattern likely results from more concentrated stress distribution at the corners, leading to a greater number of cracks after loading. However, this scenario may also be caused by the difference in the distribution morphology of the nodules within the model. The exact reason for this needs to be elucidated in a follow-up study.
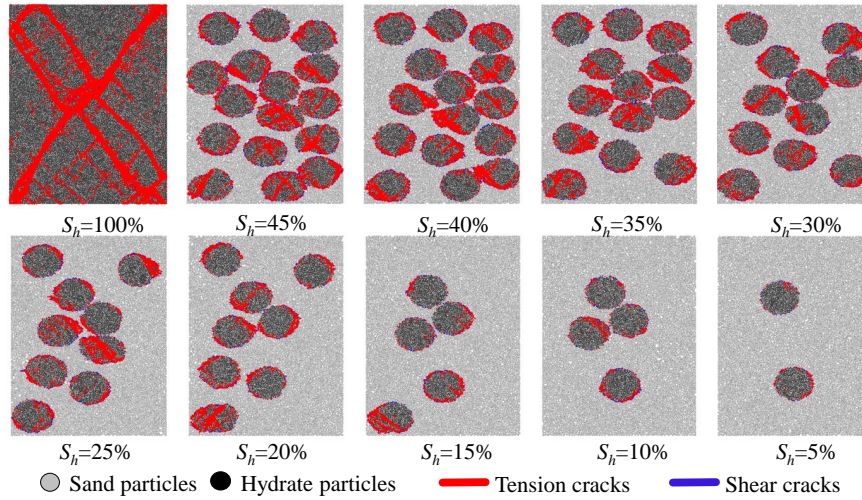
Fig. 11. State of samples with different hydrate saturation conditions after numerical simulation.

Table 2. The number of cracks developed under different saturation conditions.

S_h (%)	Tension cracks	Shear cracks	Total cracks
5	310	66	376
10	987	163	1,150
15	2,025	236	2,261
20	4,765	427	5,192
25	5,550	535	6,085
30	6,805	642	7,447
35	9,556	810	10,366
40	12,224	980	13,204
45	15,071	1,724	16,795

Table 3. The peak stresses of the model with different saturation conditions.

S_h (%)	Peak stress under confining pressures (MPa)			
	5 MPa	3 MPa	2 MPa	1 MPa
5	4.589	3.781	3.333	2.902
10	4.587	3.905	3.466	2.920
15	5.093	4.253	3.908	3.308
20	5.529	4.549	3.980	3.431
25	5.810	4.969	4.336	3.619
30	6.336	5.198	4.590	3.897
35	6.591	5.406	4.851	4.072
40	7.132	5.796	5.184	4.297
45	7.367	6.223	5.456	4.550

3.2 Confining pressure effect

Similarly, it found that the confining pressure (σ_c') in the hydrate-generating environment also affected the mechanical properties of the NGH-bearing sediment. To verify this, we analyzed the numerical simulation results of nodular gas hydrate-bearing sediment at different confining pressures. The peak values of the stress-strain curves under different saturation degrees and different confining pressures in the simulation results were shown in Table 3.

Through the analysis of the simulation results and the stress-strain curves of the model under different confining pressures and $S_h = 35\%$ as shown in Fig. 12, it further verified that the failure strength of the hydrate sediment was proportional to the confining pressure, and the larger the confining pressure, the greater the stress required for the failure of the model, and the higher the mechanical strength. Fig. 12 shows that the stress-strain curve of the model had a strain-softening phenomenon when $\sigma_c' = 1$ MPa. However, with the increase of confining pressure, this phenomenon became less apparent, and with the further increase of confining pressure, when $\sigma_c' = 5$ MPa, the strain-softening phenomenon tended to be strain hardening Li et al. (2011b) found that the failure strength of hydrate-bearing sediment increased with increasing confining pressure; this is consistent with the findings of this study. It further confirmed that the mechanical properties of different types of gas hydrate-bearing sediment were comparable.

Similarly, the simulation results indicate that, with increasing confining pressure and saturation, the strain-softening phenomenon became less apparent in the stress-strain curve. When the saturation and the confining pressure were higher, the stress-strain curve exhibited strain hardening in advance. When the saturation was low, the effect of confining pressure on crack formation was not evident; however, it became more apparent as the saturation increased. The confining pressure
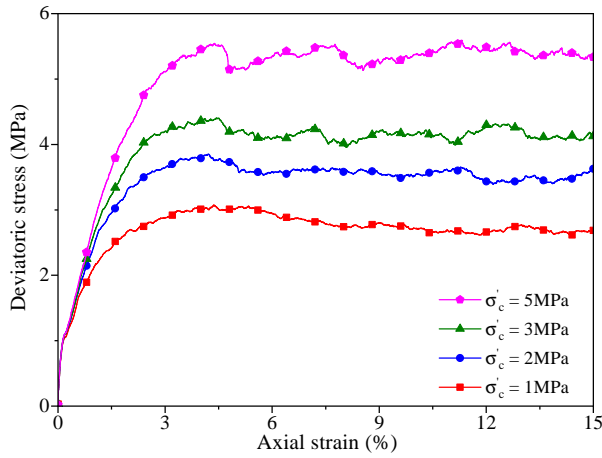
Fig. 12. Stress-strain curves at S_h = 35% and d = 0.22 mm under different confining pressures.

Table 4. The number of cracks developed with different saturation conditions.

| S_h (%) | Crack number under confining pressures | | | |
	5 MPa	3 MPa	2 MPa	1 MPa
5	1,454	1,321	1,003	376
10	2,121	2,551	1,824	1,150
15	2,483	3,552	2,803	2,277
20	7,541	6,998	6,290	5,213
25	6,532	7,739	7,990	5,550
30	8,445	7,408	7,260	6,805
35	11,534	11,228	10,866	9,556
40	14,336	14,173	13,463	12,224
45	15,292	15,064	16,795	13,047
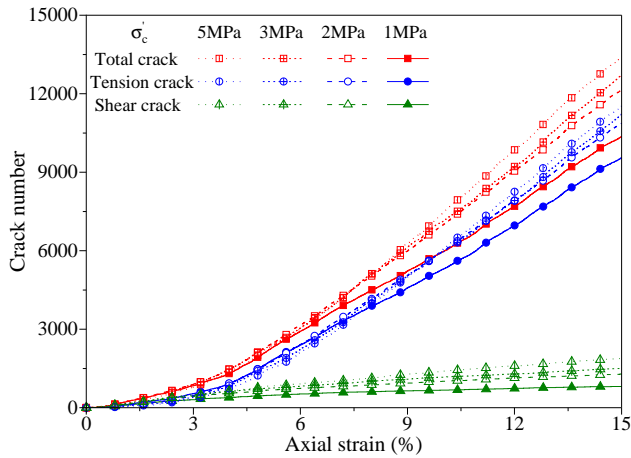
Fig. 13. Number of cracks developed at S_h = 35% and d = 0.22 mm under different confining pressures.
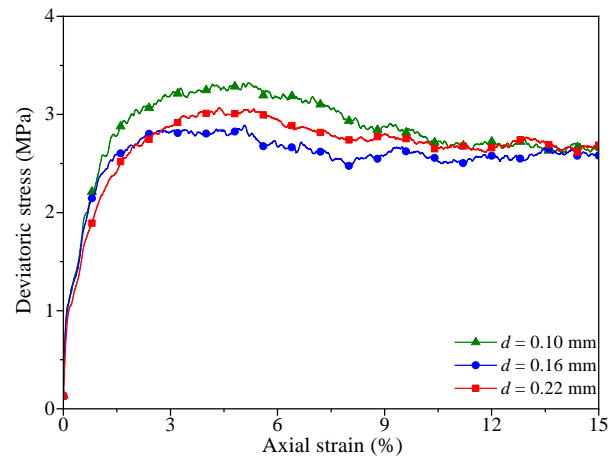
Fig. 14. Stress-strain curve at S_h = 35% and σ_c' = 1 MPa under different nodule radius conditions.

exhibited a clear positive correlation with the number of cracks in the sample (i.e., the crack formation rate).

After the simulation, the crack development curves of the model under different confining pressures, as shown in Fig. 13, did not produce cracks for a while at the beginning of the simulation. Still, with the increased confining pressure, the corresponding axial strain decreases when the crack occurs, while tensile cracks still dominate the crack type. The proportion of tensile cracks increased with the increase of confining pressure; this also verified that the mechanical strength of hydrate increases with the increase of confining pressure.

The crack development of the model under different saturation and confining pressure conditions was extracted and summarized in Table 4. From this, it is clear that when σ_c' = 1 MPa, the number of cracks generated in the model of all saturation degrees was the least, and when $1 \leq \sigma_c' \leq 3$ MPa, the number of cracks inside the model increases with the increase of confining pressure. However, when σ_c' slowly tended to 5 MPa, the number of cracks generated in the model gradually tends to be maximized, and there were no new cracks generated. Thus, higher confining pressures yielded greater failure intensities in nodular gas hydrate-bearing sediment.

3.3 Effect of nodule size

When the nodular particle size d = 0.1 mm, the stress required for model failure was the largest, and with the increase of nodular particle size, the stress required for model failure became increasingly smaller and gradually tended to a stable value as shown in Fig. 14. Simultaneously, this study still selected the crack development of the three nodular particle sizes at S_h = 35% and plots the curve shown in Fig. 15, as the above conclusion was obtained when the nodular particle size d = 0.1 mm, the number of cracks generated in the model was the largest. It was also the earliest crack in the three nodular particle size models. With the continuous increase of the nodular particle size, the influence on the crack development in the model would become less and less. Considering that the size of the model is fixed, the spatial distribution and number of hydrate nodules in the adjacent nodular particle size model are very close after the nodular particle size increases to a certain extent, and the influence on the mechanical strength of hydrate is also getting smaller and
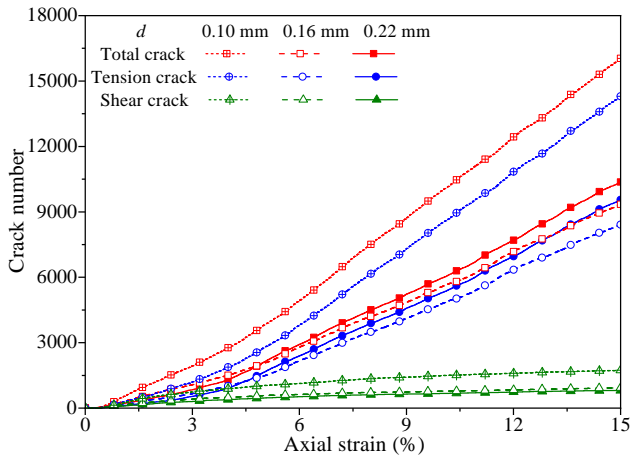
Fig. 15. Number of cracks developed at S_h = 35% and σ_c' = 1 MPa under different nodule radius conditions.

Table 5. The peak stresses of the model with different saturation conditions.

S_h (%)	Peak stress under nodular particle sizes (MPa)		
	0.10 mm	0.16 mm	0.22 mm
5	2.848	2.885	2.902
10	3.076	3.023	2.920
15	3.212	3.153	3.311
20	3.372	3.350	3.431
25	3.761	3.608	3.619
30	3.925	3.781	3.897
35	4.323	3.891	4.072
40	4.467	4.190	4.297
45	4.840	4.711	4.550

smaller. Subsequent to our research, it was observed that smaller particle sizes in the nodule correlates with increased mechanical strength in the hydrate model. However, with the increase in nodular particle size, the difference in the number and spatial distribution of hydrate nodules in the model decreased, and the influence of nodule size on the damage intensity of nodule gas hydrate sediments became less and less. Owing to the lack of a unified standard, the nodule particle sizes (d) in the simulations were set as 1.0, 1.6, and 2.2 mm. Models with different saturations and particle sizes were run at 1 MPa confining pressure. The stress-strain relationship at the same saturation and changes in the stress-strain relationship under changing saturation levels were simulated for these three particle sizes. The crack development curves were also simulated. A corresponding saturation condition diagram was drawn to explore the influence of particle size on crack development. In addition, the peak stress in the stress-strain curve obtained by extracting and simulating was plotted as Table 5, and the crack development curves of different nodular particle sizes under three different particle sizes were numer-

Table 6. Number of cracks developed with different saturation conditions.

S_h (%)	Crack number under nodular particle sizes		
	0.10 mm	0.16 mm	0.22 mm
5	1,431	547	372
10	2,942	1,490	1,147
15	4,914	3,103	2,277
20	7,842	5,068	5,213
25	9,978	7,702	5,550
30	13,493	8,080	6,805
35	15,981	9,342	1,0366
40	16,881	13,077	12,224
45	20,583	16,135	14,157

ically simulated. The number of cracks inside the model after the simulation was extracted, as shown in Table 6. When S_h > 20%, the peak stress of the hydrate model in the simulation test decreases with the increase of radius, the axial strain and crack number also decrease. This may be because of the increase in the number of nodules due to the decrease in nodule size under the same saturation conditions. This, in turn, increases the contact between the hydrate and the sand particles, and the force required for failure and deformation also increases. However, from the data shown in Table 6, the number of cracks generated in the model decreases with the increase of nodular particle size. However, with the increase of saturation, the influence of nodular particle size on the number of cracks would gradually decrease; this may be attributed to the increase of saturation leading to the increase of the number of nodules in the model when the saturation was sufficient, the spatial distribution of hydrates in the models of the three nodular particle sizes tended to be consistent. The influence of nodular particle size became increasingly smaller.

3.4 Evolution of shear zones

To explore the mechanism by which the shear zone inside the model formed, numerical simulations were performed at 45% and 100% saturations and a confining pressure of 1 MPa. The formation of the shear zone at the strain of 0-14% was shown in Fig. 16. When the axial strain was between 0 and 8% (i.e., the strain hardening stage), micro-shear zones were generated locally in the model, and the sample exhibited shear dilation. During the strain-softening stage (ε = 4%-15%), the shear zones were completely formed and the particle distribution in the shear zones was relatively scattered, with a considerable increase in porosity. However, no considerable change in the particle distribution was observed in areas far from the shear zones, and the changes in porosity in these areas were relatively small.

When S_h = 45%, cracks in the nodular NGH-bearing sediment began to form around the edges of the nodules and the points where the sand particles were cemented; this
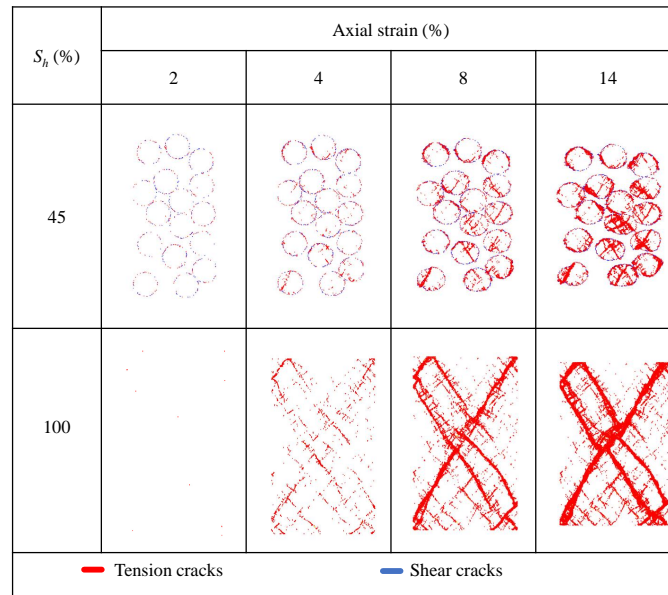
Fig. 16. Evolution process of the shear band inside the model at S_h = 45% and S_h = 100%.

intensified with increasing strain. When ε = 8%, a "\" shaped shear zone appeared inside the nodule, and when ε = 14%, an "X" shaped shear zone began to appear. When S_h = 100%, the hydrate sample experienced a strain of ε = 8% and a more distinct "X" type shear zone appeared. As the strain increased, the shear zones also deepened. In addition, some blocks of the sample slid along the directions of the shear zones.

The volumetric strain curve of the nodular NGH-bearing sediment at S_h = 45% (Fig. 9) shows that the shear expansion effect occurred when shear zones formed. In addition, the particle distribution near the shear zones was scattered, thereby increasing the porosity. Therefore, we concluded that the shear expansion effect was mainly caused by localized porosity increases in the shear zones.

4. Conclusions

In this study, it analyzed the influences of different nodule morphological characteristics on nodular NGH-bearing sediment. Mechanical simulations of round nodular NGH-bearing sediment were conducted using the PFC2D software to investigate the effects of hydrate saturation, confining pressure, and hydrate nodule radius on the mechanical properties and failure strength of heterogeneous nodular NGH-bearing sediment. In addition, the stress-strain, fracture development, and partial body strain curves, as well as the force chain distribution, were analyzed. The following conclusions were drawn:

1) The mechanical strength of the nodular NGH-bearing sediment was proportional to the gas hydrate saturation. The number of fractures also increased with increasing saturation. Compared with dispersed gas hydrate-bearing sediment, the nodular NGH-bearing sediment model primarily formed tensile cracks in fractures.
2) The volume change laws of different gas hydrate types are essentially the same: Shear shrinkage was followed by shear expansion, with the shear expansion being more

pronounced at higher gas hydrate saturation levels. The shear expansion effect of the gas hydrate saturation was not evident at 0-10% but became more apparent as the saturation increased.
3) The mechanical strength of the nodular NGH-bearing sediment was proportional to the simulated confining pressure, that is, the sample strength increased with increasing confining pressure. The strain-softening phenomenon at 1 MPa confining pressure gradually exhibited strain hardening as the confining pressure increased, and the number of cracks increased with increasing saturation.
4) When the gas hydrate saturation exceeded 20%, the failure strength of the sediment and the number of cracks both decreased with increasing particle radius. However, this phenomenon was less apparent at higher saturation levels. When $S_h \leq$ 20%, the effect of the hydrate nodule radius on the failure strength of the sediment could be overlooked; however, the radius still influenced crack formation. This effect gradually weakened with increasing saturation.
5) Porosity changes inside the sediment are crucial in the formation and evolution of shear zones. Specifically, the porosities around the shear zones were higher.

This study provides a new method for investigating the mechanical properties of nodular NGH-bearing sediment. The findings can be used to provide ideas and methodologies for future research. Although it is difficult to generate nodular NGH-bearing sediment in the laboratory, future studies should consider experimental methods of generating nodular NGH-bearing sediment.

Acknowledgements

Conflict of interest

The authors declare no competing interest.

References

Aregbe, A. G. Gas hydrate-properties, formation and benefits. Open Journal of Yangtze Oil and Gas, 2017, 2(1): 27-44.

Bai, B., Zhou, R., Yang, G., et al. The constitutive behavior and dissociation effect of hydrate-bearing sediment within a granular thermodynamic framework. Ocean Engineering, 2023, 268: 113408.

Boswell, R. Engineering. Is gas hydrate energy within reach? Science, 2009, 325(5943): 957-958.

Boswell, R., Collett, T. S. Current perspectives on gas hydrate resources. Energy & Environmental Science, 2011, 4(4): 1206-1215.

Brugada, J., Cheng, Y. P., Soga, K., et al. Discrete element modelling of geomechanical behaviour of methane hydrate soils with pore-filling hydrate distribution. Granular Matter, 2010, 12(5): 517-525.

Collett, T. S. Energy resource potential of natural gas hydrates. AAPG Bulletin, 2002, 86(11): 1971-1992.

Collett, T. S., Kuuskraa, V. A. Hydrates contain vast store of world gas resources. Oil and Gas Journal, 1998, 96(19): 90-94.

Dai, S., Seol, Y. Water permeability in hydrate-bearing sediments: A pore-scale study. Geophysical Research Letters, 2014, 41(12): 4176-4184.

Demirbas, A. Methane hydrates as potential energy resource: Part 1-importance, resource and recovery facilities. Energy Conversion and Management, 2010, 51(7): 1547-1561.

Dong, L., Wu, N., Zhang, Y., et al. Improved duncan-chang model for reconstituted hydrate-bearing clayey silt from the south china sea. Advances in Geo-Energy Research, 2023, 8(2): 136-140.

Gong, B., Jiang, Y., Yan, P., et al. Discrete element numerical simulation of mechanical properties of methane hydrate-bearing specimen considering deposit angles. Journal of Natural Gas Science and Engineering, 2020, 76: 103182.

Gong, B., Zhang, R., Sun, T., et al. Coupling model of submarine deformation response prediction during methane hydrate exploitation. Energy & Fuels, 2022, 36(13): 6785-6809.

Hyodo, M., Li, Y., Yoneda, J., et al. Mechanical behavior of gas-saturated methane hydrate-bearing sediments. Journal of Geophysical Research: Solid Earth, 2013, 118(10): 5185-5194.

Hyodo, M., Nakata, Y., Yoshimoto, N., et al. Bonding strength by methane hydrate formed among sand particles. Paper Presented at Powders and Grains 2009: Proceedings of the 6th International Conference on Micromechanics of Granular Media, 13-17 July, 2009.

Itasca, C. G. Pfc-pfc 6.0 documentation. Itasca Consulting Group Minneapolis, MN, 2018.

Jensen, R. P., Bosscher, P. J., Plesha, M. E., et al. Dem simulation of granular media-structure interface: Effects of surface roughness and particle shape. International Journal for Numerical and Analytical Methods in Geomechanics, 1999, 23(6): 531-547.

Jiang, M., Liu, J., Shen, Z. Dem simulation of grain-coating type methane hydrate bearing sediments along various stress paths. Engineering Geology, 2019, 261: 105280.

Jiang, M., Peng, D., Ooi, J. Y. Dem investigation of mechanical behavior and strain localization of methane hydrate bearing sediments with different temperatures and water pressures. Engineering Geology, 2017, 223: 92-109.

Jiang, Y., Gong, B. Discrete-element numerical modelling method for studying mechanical response of methane-hydrate-bearing specimens. Marine Georesources & Geotechnology, 2020, 38(9): 1082-1096.

Kumar, P., Sonawane, A. Engineering significance and consequences of gas hydrates in deep and ultra deep water development. Paper ISOPE-I-04-042 Presented at ISOPE International Ocean and Polar Engineering Conference, Toulon, France, 23-28 May, 2004.

Li, Y., Dong, L., Wu, N., et al. Influences of hydrate layered distribution patterns on triaxial shearing characteristics of hydrate-bearing sediments. Engineering Geology, 2021a, 294: 106375.

Li, Y., Li, J., You, Z., et al. A particle-scale investigation of mechanical behavior of cemented hydrate-bearing sediment using discrete element method. Geomechanics for Energy and the Environment, 2023, 33: 100436.

Li, Y., Liu, L., Jin, Y., et al. Characterization and development of natural gas hydrate in marine clayey-silt reservoirs: A review and discussion. Advances in Geo-Energy Research, 2021b, 5(1): 75-86.

Li, Y., Song, Y., Yu, F., et al. Effect of confining pressure on mechanical behavior of methane hydrate-bearing sediments. Petroleum Exploration and Development, 2011a, 38(5): 637-640.

Li, Y., Song, Y., Yu, F., et al. Experimental study on mechanical properties of gas hydrate-bearing sediments using kaolin clay. China Ocean Engineering, 2011b, 25(1): 113-122.

Linga, P., Clarke, M. A. A review of reactor designs and materials employed for increasing the rate of gas hydrate formation. Energy & Fuels, 2016, 31(1): 1-13.

Liu, H., Guo, P., Zhan, S., et al. Experimental investigation into formation/dissociation characteristics of methane hydrate in consolidated sediments with resistance measurement. Fuel, 2018, 234: 985-995.

Madhusudhan, B. N., Clayton, C. R. I., Priest, J. A. The effects of hydrate on the strength and stiffness of some sands. Journal of Geophysical Research: Solid Earth, 2019, 124(1): 65-75.

Makogon, Y. F., Holditch, S. A., Makogon, T. Y. Natural gas-hydrates — a potential energy source for the 21st

century. Journal of Petroleum Science and Engineering, 2007, 56(1-3): 14-31.

Masui, A., Miyazaki, K., Haneda, H., et al. Mechanical characteristics of natural and artificial gas hydrate bearing sediments. Paper ICGH 2008 Presented at the 6th International Conference on Gas Hydrates, Vancouver, British Columbia, Canada, 6-10 July, 2008.

Miyazaki, K., Masui, A., Tenma, N., et al. Study on mechanical behavior for methane hydrate sediment based on constant strain-rate test and unloading-reloading test under triaxial compression. International Journal of Offshore and Polar Engineering, 2010, 20(1): 61-67.

Moridis, G. J., Collett, T. S., Pooladi-Darvish, M., et al. Challenges, uncertainties, and issues facing gas production from gas-hydrate deposits. SPE Reservoir Evaluation & Engineering, 2011, 14(1): 76-112.

Ning, F., Liang, J., Wu, N. Reservoir characteristics of natural gas hydrates in China. Natural Gas Industry, 2020, 40(8): 1-25. (in Chinese)

Priest, J. A., Hayley, J. L., Smith, W. E., et al. Pcats triaxial testing: Geomechanical properties of sediments from pressure cores recovered from the bay of bengal during expedition nghp-02. Marine and Petroleum Geology, 2019, 108: 424-438.

Rutqvist, J., Moridis, G. J., Grover, T., et al. Geomechanical response of permafrost-associated hydrate deposits to depressurization-induced gas production. Journal of Petroleum Science and Engineering, 2009, 67(1-2): 1-12.

Seol, J., Lee, H. Natural gas hydrate as a potential energy resource: From occurrence to production. Korean Journal of Chemical Engineering, 2013, 30(4): 771-786.

Sloan, E. D. Clathrate hydrate measurements: Microscopic, mesoscopic, and macroscopic. The Journal of Chemical Thermodynamics, 2003, 35(1): 41-53.

Vinod, J., Hyodo, M., Indraratna, B., et al. Dem modelling of methane hydrate bearing sand. Australian Geomechanics Journal, 2014, 49(4): 175-182.

Wan, Y., Yuan, Y., Zhou, C., et al. Multiphysics coupling in exploitation and utilization of geo-energy: State-of-the-art and future perspectives. Advances in Geo-Energy Research, 2023, 10(1): 7-13.

Wang, D., Ning, F., Lu, J., et al. Reservoir characteristics and critical influencing factors on gas hydrate accumulations in the Shenhu area, South China sea. Marine and Petroleum Geology, 2021a, 133: 105238.

Wang, H., Chen, Y., Zhou, B., et al. Investigation of the effect of cementing ratio on the mechanical properties and strain location of hydrate-bearing sediments by using dem. Journal of Natural Gas Science and Engineering, 2021b, 94: 104123.

Wang, X., Sun, Y., Li, B., et al. Reservoir stimulation of marine natural gas hydrate-a review. Energy, 2023, 263:

126120.

Whiticar, M. J., Faber, E., Schoell, M. Biogenic methane formation in marine and freshwater environments: CO_2 reduction vs. Acetate fermentation—isotope evidence. Geochimica et Cosmochimica Acta, 1986, 50(5): 693-709.

Winters, W. J., Waite, W. F., Mason, D. H., et al. Methane gas hydrate effect on sediment acoustic and strength properties. Journal of Petroleum Science and Engineering, 2007, 56(1-3): 127-135.

Wu, Q., Dou, X., Zhao, Y., et al. Discrete element simulation of the hydrate-bearing sediments mechanical behaviors under typical hydrate dissociation patterns. Gas Science and Engineering, 2023, 115: 205020.

Yang, Q., Zhao, C. Three-dimensional discrete element analysis of mechanical behavior of methane hydrate-bearing sediments. Rock and Soil Mechanics, 2014, 35(1): 255-262. (in Chinese)

Yoneda, J., Kida, M., Konno, Y., et al. In situ mechanical properties of shallow gas hydrate deposits in the deep seabed. Geophysical Research Letters, 2019, 46(24): 14459-14468.

You, Z., Wu, P., Sun, X., et al. Effect of hydrate distribution on the mechanical response of hydrate-bearing sand: Discrete element method simulation. Energy & Fuels, 2022, 36(7): 3802-3815.

Yun, T. S., Santamarina, J. C., Ruppel, C. Mechanical properties of sand, silt, and clay containing tetrahydrofuran hydrate. Journal of Geophysical Research: Solid Earth, 2007, 112(B4): B04106.

Zeng, S., Mao, L., Liu, Q., et al. Study on mechanical properties of natural gas hydrate production riser considering hydrate phase transition and marine environmental loads. Ocean Engineering, 2021, 235: 109456.

Zhang, G., Liang, J., Yang, S., et al. Geological features, controlling factors and potential prospects of the gas hydrate occurrence in the east part of the pearl river mouth basin, South China sea. Marine and Petroleum Geology, 2015, 67: 356-367.

Zhang, N., Wang, H. N., Jiang, M. J. A mesoelastic-plastic damage model for hydrate-bearing sediments with various hydrate-growth patterns. Ocean Engineering, 2022, 266: 112919.

Zhang, X., Lu, X., Li, Q., et al. Thermally induced evolution of phase transformations in gas hydrate sediment. Science China Physics, Mechanics and Astronomy, 2010, 53: 1530-1535.

Zhao, M., Liu, H., Ma, Q., et al. Discrete element simulation analysis of damage and failure of hydrate-bearing sediments. Journal of Natural Gas Science and Engineering, 2022, 102: 104557.